Probing spin-orbit-interaction-induced electron dynamics in the carbon atom by multiphoton ionization

Published in:
Physical Review A (Atomic, Molecular, and Optical Physics)

Document Version:
Peer reviewed version

Queen's University Belfast - Research Portal:
Link to publication record in Queen's University Belfast Research Portal

Electron dynamics in the carbon atom induced by spin-orbit interaction

H.F. Rey[1, *] and H.W. van der Hart[1]

[1]*Centre for Theoretical Atomic, Molecular and Optical Physics, School of Mathematics and Physics*
Queen's University Belfast, Belfast BT7 1NN, United Kingdom

(Dated: September 9, 2014)

We use R-Matrix theory with Time dependence (RMT) to investigate multiphoton ionization of ground-state atomic carbon with initial orbital magnetic quantum number $M_L = 0$ and $M_L = 1$ at a laser wavelength of 390 nm and peak intensity of 10^{14} W cm^{-2}. Significant differences in ionization yield and ejected-electron momentum distribution are observed between the two values for M_L. We use our theoretical results to model how the spin-orbit interaction affects electron emission along the laser polarization axis. Under the assumption that an initial C atom is prepared at zero time delay with $M_L=0$, the dynamics with respect to time delay of an ionizing probe pulse modeled using RMT theory is found to be in good agreement with available experimental data.

I. INTRODUCTION

Over the last 15 years great advances have been made in the development and application of experimental laser techniques on the sub-femtosecond time-scale (1 fs = 10^{-15} s) [1]. These advances have the prospect of the detailed study and potential guiding of electron motion in atoms and molecules. Several methods have been applied to monitor the electron dynamics, such as pump-probe spectroscopy using few-cycle pulses, through which, for example, the angular correlation between sequential ionization steps was investigated [2]. Another example is transient absorption spectroscopy, in which, for example, sequential ionization dynamics of Kr was investigated [3]. This experiment demonstrated the influence of the spin-orbit interaction on the Kr$^+$ dynamics when sufficiently short ionization pulses are employed.

Electron motion in a general atom can be regarded as the complement of atomic structure via the time-energy uncertainty principle. In the atomic structure of light atoms, relativistic interactions, such as spin-orbit coupling, are normally assumed to be negligible. However, in heavier atoms, this assumption no longer holds. As a consequence, it can be assumed that spin-orbit dynamics may have a relatively minor effect on electron dynamics of light atoms on the time scale of a short laser pulse, whereas this dynamics will become important when heavier atoms are considered. That does not mean, however, that spin-orbit dynamics is irrelevant for light atoms: when light atoms interact with a sequence of two light pulses with a long time delay between the two, spin orbit dynamics can affect the intermediate state significantly [4, 5].

Changes in the atomic state induced by spin-orbit interaction can affect the subsequent atomic dynamics significantly [6]. Total angular momentum $J = L + S$, with L total orbital angular momentum and S total spin, is conserved, as is its projection on the z-axis, $M_J = M_L + M_S$. However, although M_J is conserved, its components M_L and M_S are not. Hence, the spin-orbit interaction can change, for example, a JM_JLS state with $M_L = 0$ and $M_S = +1/2$ into a JM_JLS state with $M_L = +1$ and $M_S = -1/2$. This change in orbital magnetic quantum number can have a noticeable effect on the atomic dynamics: For example, in harmonic generation of noble-gas ions Ne$^+$ and Ar$^+$, the harmonic yields for $M_L = 0$ were reduced by a factor 2-4 compared to $M_L = \pm1$ [7, 8].

Recently, pump-probe experiments have been carried out to investigate the spin-orbit induced dynamics in the C ground state following photodetachment of C$^-$ [4, 5]. In these studies, an initial C atom was formed by photodetachment of C$^-$. This residual C atom is left in a superposition of ground state ^{3}P^e levels with different J. The energy splitting between the different J levels then leads to dynamics within the different M_L levels, which can be observed through differences in the measured ejected-electron momentum spectra between parallel polarization of the pump and probe pulses and perpendicular polarization of the pulses. These differences were shown to vary with a period of 760 to 2000 fs, as can be deduced from the energy difference between the J levels of the C ^{3}P^e ground state, 2.0 meV between the lower $J = 0$ and the $J = 1$ level, and 3.4 meV between the $J = 1$ and $J = 2$ level [9].

From a theoretical perspective, the influence of relativistic interactions on ultra-fast atomic dynamics has already been the subject of theoretical investigation [10, 11]. However, it would be very useful to develop this capability in other theoretical methods and techniques as well, such as, for example, time-dependent R-matrix theory [12–15]. The most recent implementation of time-dependent R-matrix theory, named R-matrix theory including time dependence (RMT), is the most efficient implementation for large-scale studies, as it provides better stability when many angular momenta are included and provides better scope for exploitation of massively parallel computing facilities. The first step in this development

*Electronic address: h.rey@qub.ac.uk

is to verify that initial states with $M_L \neq 0$ can be investigated accurately using the RMT approach. However, whereas the previous implementation of time-dependent R-matrix theory has already been applied to the investigation of dynamics for atoms with $M_L \neq 0$ [7, 8, 16], up to now RMT theory has only been applied to systems with $M_L = 0$ [17, 18].

In this report, we demonstrate that RMT theory can be applied to the study of atoms with an initial $M_L \neq 0$. We apply the theory to investigate ejected-electron momentum distributions for the multiphoton ionization of C atoms in short 390-nm laser pulses with a peak intensity of 10^{14} W/cm^2 for both $M_L = 0$ and $M_L = 1$. We will explain the significant changes in these momentum distributions between the two values of M_L. We then use these momentum distributions to model the observation of spin-orbit dynamics in C as a function of time delay τ for the ionization pulse, under the assumption that a ground-state C atom is created at time $t = 0$ by emission of an $m_\ell = 0$ electron from ground-state C$^-$. Since the spin-orbit dynamics in C occurs on timescales longer than the duration of the 390-nm laser pulse, which takes 1.3 fs per cycle, it can be assumed that no spin-orbit dynamics occurs during the interaction with the laser pulse. The time-delayed initial state of C can then be regarded as a superposition of states with $M_L = 1$, $M_L = 0$, and $M_L = -1$.

The organisation of the report is as follows. In Sec. II, we give a brief overview of RMT theory, including a description of changes required to treat non-zero M. The specific parameters used in the present calcutations, including a description of the C$^+$ basis set, are also included. In Sec. III, we present our calculated ejected-electron momentum distributions along with seleceted photoelectron energy spectra focusing on the differences seen for $M_L = 0$ and $M_L = 1$. We then model the differences in the ejected-electron momentum spectra that would be induced by spin orbit dynamics, and compare these with the experimental findings [4, 5]. Finally in Sec IV, we report our conclusions.

II. METHODS

A. The RMT approach

In this report, we employ the RMT approach to investigate multiphoton ionization of neutral carbon and model the ejected electron dynamics. The RMT method builds upon traditional R-matrix theory [19, 20], by separating the description of the system into two distinct regions: an inner region and an outer region. In the inner region, the wavefunction is expressed in terms of a multi-electron R-matrix basis description within a confined spatial region surrounding the nucleus [20]. In the outer region, the full multi-electron wavefunction is descibed as a direct product of a channel function and a finite-difference representation of the single-electron radial wavefunction for an outer elecron found only outside the confined spatial region [14, 15]. The channel function comprises the wavefunction of a residual-ion state coupled with the spin and angular momentum functions of the ejected electron.

A key feature of the RMT approach is the connection between the inner and outer regions. To provide information about the inner-region wavefunction to the outer region, the outer-region grid is extended into the inner region. The inner-region radial wavefunction is then evaluated on this grid extension, and made available to the outer region. In order to provide outer-region wavefunction information to the inner-region, time derivatives of the outer-region wavefunction are evaluated at the inner-region boundary, and are then provided to the inner-region. Full details about the link between the two regions are provided in [14, 15].

Time propagation within the RMT approach is carried out through Arnoldi propagators [21]. Through the grid extension into the inner region, all the necessary information for propagation of the outer-region wavefunction is available on the outer-region grid, and the propagation through an Arnoldi propagator is relatively straightforward. In the inner region, however, different Arnoldi propagators are needed for the wavefunction, and for each outer-region time derivative at the boundary. All time derivatives are therefore propagated separately, and the full time-propagated wavefunction is obtained by combining all the separate propagation terms [14, 15].

The implementation of the RMT codes to date was limited to systems with an initial angular momentum $L = 0$ and, consequently, $M_L = 0$. However, the ground state of C has ^{3}P^e symmetry which can have a total magnetic quantum number $M_L = -1, 0$, or 1. The value of M_L significantly affects the calculations. According to dipole selection rules, only transitions with $\Delta L = \pm 1$ are allowed for $M_L = 0$. On the other hand, for $M_L = 1$, transitions with $\Delta L = 0$ are allowed in addition to $\Delta L = \pm 1$. As a consequence, for $M_L = 0$, only a single parity needs to be included for each value of L, whereas for $M_L = 1$, both parities need to be included for each value of L. More symmetries are therefore available for $M_L = 1$ and the calculations approximately double in size. In addition, we need to take into account that all symmetries can now potentially interact with three other symmetries, rather than two. Within the parallel implementation of the RMT codes, this requires additional communication between MPI tasks. However, since the propagation involves only matrix-vector multiplications, no reordering of the symmetry blocks is required, in contrast to the previous implementation of time-dependent R-matrix theory [16].

B. The description of C

To study the influence of the initial value of M_L values on the multiphoton ionization dynamics of C, we employ

TABLE I: C^+ threshold energies relative to the ground state of C, compared to literature values [9]. Energies are not given for the $2p^3$ states as these lie inbetween the $2s^2 3\ell$ and $2s^2 4\ell$ states. Apart from the energy for the $2s2p^2$ $^2S^e$ state, all present energies agree with those in [22].

C^+ state	Present energy	Literature [9]
	eV	eV
$2s^2 2p$ $^2P^o$	11.366	11.262
$2s2p^2$ $^4P^e$	16.430	16.592
$2s2p^2$ $^2D^e$	20.962	20.547
$2s2p^2$ $^2S^e$	24.196	23.220
$2s2p^2$ $^2P^e$	25.706	24.976

an R-matrix basis set previously employed to investigate photoionization of C [22]. In this basis set, all possible residual ion states are considered that can be formed using 2s and 2p orbitals:

$$n\hbar\omega + C(2s^2 2p^2\ {}^3P^e) \rightarrow C^+(2s^2 2p\ {}^2P^o) + e^-$$
$$\rightarrow C^+(2s2p^2\ {}^{2,4}P^e, {}^2D^e, {}^2S^e) + e^-$$
$$\rightarrow C^+(2p^3\ {}^4S^o, {}^2D^o, {}^2P^o) + e^-$$

The 1s, 2s and 2p orbitals building these three ionic configurations are given by the 1s, 2s and 2p Hartree-Fock orbitals for the $^2P^o$ ground state of the ion [23]. To improve the description of the C^+ eigenstates, the basis set also includes $\overline{3s}$, $\overline{3p}$, and $\overline{3d}$ pseudo-orbitals orthogonal to the Hartree-Fock orbitals. The C^+ basis set is then expanded by allowing single excitations from the $2s^2 2p$, $2s2p^2$ and $2p^3$ configurations to these pseudo-orbitals. Energies of the lowest five eigenstates of C^+ are given in table I and compared with literature values [9]. The energies of the $2p^3$ states are not given, as they lie above the $2s^2 3s$ states, which have been excluded from the present calculations. The energies agree exactly with those obtained in [22], apart from the energy for the $2s2p^2$ $^2S^e$ state. This is most likely due to a small difference in the CI expansion used for this state, which includes 6 basis functions in the present calculations, whereas the one reported in [22] includes 5 basis functions. The table demonstrates that the lowest two thresholds are within 0.2 eV of the literature values, whereas the differences increase rapidly for the higher states. This is not surprising as the $2s2p^2$ $^2D^e$ and $^2S^e$ states will interact strongly with the physical $2s^2 3d$ and $2s^2 3s$ states, respectively. The $\overline{3s}$ and $\overline{3d}$ orbitals used in the present calculations are pseudo-orbitals, and will therefore not accurately reflect the 3s and 3d orbitals in the physical states. Hence the interaction with $2s^2 3d$ and $2s^2 3s$ will not be described accurately, and the obtained threshold energies will be less accurate. Nevertheless, the most important threshold states in the present multiphoton calculations are the lowest two thresholds, and these are described with sufficient accuracy for the present purposes.

The C basis set is formed by combining the eigenstates for C^+ obtained given the basis set above with a basis set describing the continuum electron. The functions in this basis set are described in terms of 65 B-splines of order $k = 11$. This basis set is augmented by correlation functions, which are created by adding one of the input orbitals to the configurations used in the description of C^+. It is further ensured that every function in the continuum basis set is orthogonal to any input orbital. The radius of the inner region was chosen to be 27 a_0. This is larger than considered in the previous C photoionization calculations, as, at present, the initial state needs to be fully contained within the inner region in the RMT approach. The C ground-state energy has not been shifted.

In the multiphoton ionization calculations, we investigate C atoms irradiated by a laser field with a wavelength of 390 nm. The total pulse length is 8 cycles, consisting of a 3-cycle $\sin^2$ ramp-on, 2 cycles at peak intensity, followed by a 3-cycle $\sin^2$ ramp-off of the electric field. Following the end of the pulse, the wavefunction is propagated field-free for another twelve cycles. For the present investigations, the peak intensity was chosen to be 10^{14} W/cm^2.

In the analysis of the final wavefunction, we only consider the outer region wavefunction, as continuum electrons are assumed to have escaped the inner region after the propagation at the end of the pulse. Within the RMT approach, the outer region wavefunction is decribed in terms of a residual ionic state plus spin and angular momentum of the outer electron coupled with a radial wavefunction for the outer electron on a discretized finite difference grid. The finite-difference grid has a grid spacing of $\Delta r = 0.15$ a_0, and extends to an outer radius of over 3900 a_0.

As indicated earlier, time propagation within the RMT approach is achieved through the use of Arnoldi propagators [21]. In the present application, we use Arnoldi propagators of order 12 with a time step of $\Delta t = 0.01$ atomic units.

III. RESULTS

The main goal in the present calculations is to study how spin-orbit dynamics affects the multiphoton ionization characteristics of ground-state carbon atoms. Since the spin-orbit dynamics in ground-state C is slow compared to the present photoionization dynamics, we can decouple the two types of dynamics and instead investigate how changes in the orbital magnetic quantum number M_L are reflected in the multiphoton ionization characteristics. We can subsequently investigate how spin-orbit dynamics changes the magnetic sublevel populations in time, and then derive the changes in the ejected-electron momentum spectra driven by the spin-orbit interaction.

A second objective of the present calculations is to investigate the convergence of the final-state populations in the different partial waves with the number of angular momenta retained in the calculation. We adopted as our convergence criterion that the final population

in each outer channel should have converged to within 0.01% of the population in the most populated channel. This convergence was achieved for a maximum angular momentum to be retained in the calculation, $L_{\max}$, of 53. We also carried out calculation with different propagation orders, and found no significant difference between propagation orders of 12 and 14. All calculations were therefore carried using an Arnoldi propagator of order 12.

The main outcomes of the calculations are shown in figures 1 and 2, which show the ejected-electron momentum distributions obtained for ground-state C atoms irradiated by 390 nm light at an intensity of 10^{14} W/cm^2 for $M_L = 0$ and $M_L = 1$, respectively. The determination of the ejected-electron momentum distributions is, however, not straightforward at this intensity. At an approximate intensity of 0.95×10^{13} W/cm^2, channel closing occurs, so that five photons are needed for ionization instead of four. However, if the bandwidth of the laser pulse is taken into account as well, both four-photon excitation of Rydberg states and four-photon ionization will occur simultaneously. To improve the separation of Rydberg-state population from continuum-state population, the system is propagated for twelve 390-nm cycles after the pulse has ended.

In the experimental analysis of the ejected-electron momentum distributions, however, the low-energy part of the distributions was not taken into account [4, 5]. We have therefore chosen to do the same in the present analysis. At the end of the calculations, we obtain the outer-region part of the final-state wavefunction. The outer electron is decoupled from the residual ion, which enables us to extract a wavefunction for the outer electron associated with each residual-ion state. We then transform the wavefunction for the outer electron for distances larger than 108 a_0 into the momentum representation under the assumption that the Coulomb potential can be neglected. This distance was chosen by examination of the final-state wavefunction. For distances greater than 108 a_0, the final-state wavefunction has clear continuum-wave characteristics, whereas this is not the case for distances smaller than 108 a_0. To examine the influence of our choice of distance, we have carried out our analysis for other distances as well. We observe that, if C$^+$ is left in the ground state, this leads to quantitative convergence of the momentum spectra for momenta greater than about 0.30 atomic units, with a good qualitative description for lower momenta. The momentum of an electron absorbing five photons is about 0.48 atomic units, and this part of the spectrum of primary interest is not affected by our choice of distance. If C$^+$ is left in the lowest excited state, the procedure leads to a good quantitative description over the entire momentum spectrum due to the absence of threshold photoelectrons. The momentum of an electron absorbing the minimum number (six) of photons is about 0.30 atomic units.

Since the C ground state has ^{3}P^e symmetry, figures 1 and 2 show the momentum distributions for an initial or-
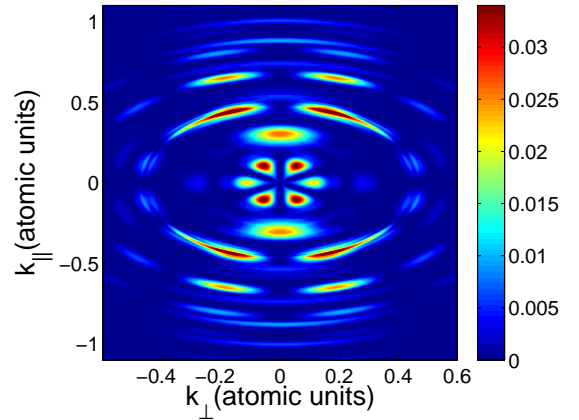

FIG. 1: (Color online) Ejected-electron momentum distribution in the $k_x k_z$-plane for C initially in the ground state with $M_L = 0$, irradiated by an 8 cycle UV laser pulse with wavelength 390 nm and intensity 10^{14} W/cm^2. The distribution includes the emission of electrons towards the lowest two states of C$^+$, which contribute over 99% to the total outer-region population in the present calculations.

bital magnetic quantum number $M_L = 0$ and $M_L = 1$, respectively. The figure clearly shows great differences between the two momentum distributions associated with the change of magnetic quantum number. For $M_L = 1$, almost all the ionization is aligned along the laser polarization axis, whereas for $M_L = 0$, two different contributions can be seen, one aligned along the laser polarisation axis and one at an angle to it.

Two different distributions can be seen in the ejected-electron momentum distributions for an initial $M_L = 0$ in figure 1. These are associated with different residual-ion states of C$^+$, or, alternatively, the ejection of different electrons. Emission along the laser polarization axis involves emission of a 2s electron, leaving C$^+$ in the excited 2s2p^2 ^{4}P^e state, whereas emission away from the laser polarization axis involves emission of a 2p electron leaving C$^+$ in its 2s^{2}2p ^{2}P^o ground state. For $M_L = 0$, the total population beyond a distance of 108 a_0, used in the determination of figure 1, in 2p emission channels is 2.86%, whereas the one in channels leaving C$^+$ in the 2s2p^2 ^{4}P^e state is 0.55%. The total population in the outer region at the end of the calculation is 4.73%, with 4.16% associated with the C$^+$ ground state and 0.56% with the first excited state of C$^+$. Higher-lying states of C$^+$ account for less than 0.4% of the total population in the outer region, and therefore the contribution to the momentum distributions from outgoing electrons attached to these states is assumed to be negligible. These populations indicate that although the majority of the population in the outer region is assigned to ionization, a significant amount of population may be associated with Rydberg-state population. The main reason for this is the proximity of the intensity used in the calculations to a channel-closing intensity.
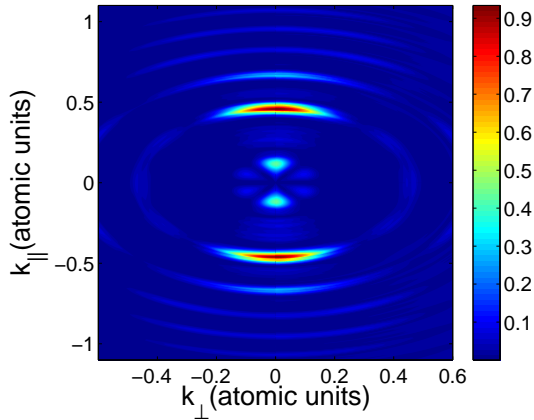
FIG. 2: (Color online) Ejected-electron momentum distribution in the $k_x k_z$-plane for C initially in the ground state with $M_L = 1$, irradiated by an 8 cycle UV laser pulse with wavelength 390 nm and intensity 10^{14} W/cm^2. The distribution includes the emission of electrons towards the lowest two states of C$^+$, which contribute over 99% to the total outer-region population in the present calculations.

The same two distributions also make up the ejected-electron momentum distributions for an initial magnetic quantum number $M_L = 1$, shown in figure 2. However, in this case, the momentum distribution is dominated by the emission of a 2p electron along the laser polarization axis. Emission of a 2s electron towards the 2s2p^2 state of C$^+$ is still possible, but it is not apparent in the present ejected-electron momentum distribution. For $M_L = 1$, the total population in 2p emission channels beyond a distance of 108 a_0 is 19.56%, whereas it is 1.06% for 2s emission channels leaving C$^+$ in the 2s2p^2 ^{4}P^e state. The total population in the outer region at the end of the calculation is 28.31%, with 27.17% associated with the C$^+$ ground state and 1.07% associated with the first excited state of C$^+$. Higher-lying states of C$^+$ account for less than 0.25% of the population in the outer region, and therefore the contribution to the momentum distributions from outer-region channels associated with these states is again assumed to be negligible. Again, the total population in the outer region is noticeably larger than the population associated with ionization. It can be seen that the total population in the outer region has increased by more than a factor 6 from the population obtained in the $M_L = 0$ calculation, with an increase in the emission probability for a 2p electron by a factor 7. The emission probability for a 2s electron has also increased, but only by a factor 2.

The reason for the difference in the ejected-electron momentum distribution is that emission of $m_\ell = 0$ electrons is strongly preferred in a linearly polarised laser field. For an initial magnetic quantum number $M_L = 0$, symmetry prevents the emission of an electron with $m_\ell = 0$, leaving C$^+$ in a 2s^{2}2p ^{2}P^o state with $M'_{L'} = M_L - m_\ell = 0$. Since transitions with $\Delta L = 0$
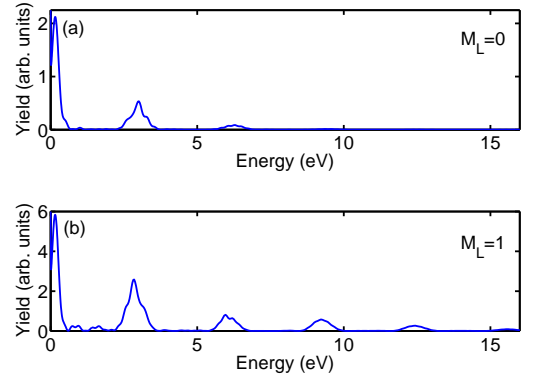

FIG. 3: (Color online) Photo-electron spectra for electrons leaving the residual C$^+$ ion in the ground state observed at an angle of 27° to the laser polarization axis for (a) $M_L = 0$ and (b) $M_L = 1$ in a laser field with a wavelength of 390 nm and peak intensity of 10^{14} W/cm^2.

are not allowed for $M_L = 0$, the only 2s^{2}2p ionization channels available are of the form 2s^{2}2p(^{2}P^o)$\varepsilon\ell$ ^{3}L with $\ell = L$. However, the Clebsch-Gordan coefficient CG(1 L L; 0 0 0) is identical to 0. On the other hand, for $M_L = 1$, emission of a 2p electron with $m_\ell = 0$ is allowed, and this process dominates the ionization.

The contribution of emission of a 2s electron to the total ionization demonstrates that above-threshold ionization is important for C at this combination of wavelength and intensity. It takes absorption of one extra photon to eject the 2s electron. This importance of above-threshold ionization is also visible in the ejected-electron momentum distributions. For emission of the 2p electron, three additional peaks at higher momentum can be seen for $M_L = 0$ and one for $M_L = 1$. For emission of a 2s electron, however, another four peaks can be seen along the laser polarization axis for $M_L = 0$.

To visualise the importance of above-threshold ionization in more detail, we can also investigate the photo-electron spectrum for a particular emission angle. The photo-electron energy spectrum associated with the 2s^{2}2p ^{2}P^o ground and ^{4}P^e excited state of the residual C$^+$ ion are shown in figures 3 and 4, respectively, for both $M_L = 0$ and $M_L = 1$. We have chosen an angle of 27° with the laser polarization axis for these energy spectra, as this allows these spectra to be studied with a reasonable magnitude for all 4 cases.

Figure 3 shows the photoelectron spectrum associated with the residual C$^+$ ion left in its ground state for initial C atoms in either $M_L = 0$ or $M_L = 1$. It can be seen that the overall magnitude of the photoelectron spectrum is significantly larger for $M_L = 1$ than it is for $M_L = 0$, which is primarily due to the increase in ionization yield for $M_L = 1$: the peak at 3 eV has increased by about a factor 5. It can furthermore be seen that the number of above threshold peaks is substantially larger for $M_L = 1$ than for $M_L = 0$. For $M_L = 0$, the above threshold
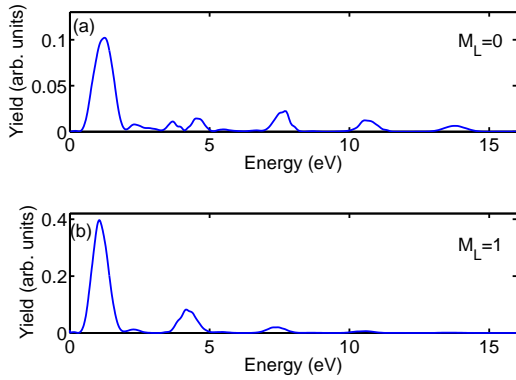
6

FIG. 4: (Color online) Photo-electron spectra for electrons leaving the residual C^+ ion in the excited $2s2p^2$ $^4P^e$ state observed at an angle of $27°$ to the laser polarization axis for (a) $M_L = 0$ and (b) $M_L = 1$ in a laser field with a wavelength of 390 nm and peak intensity of 10^{14} W/cm^2.
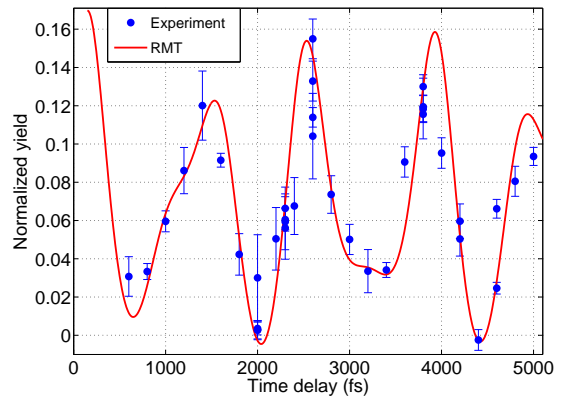
FIG. 5: (Color online) Normalized high-energy ionization yield differences as a function of time delay for C. The experimental data (circles, [5]) shows normalised ionization yield differences for energetic electrons along the probe-laser polarization axis between a probe pulse with perpendicular polarization direction and parallel polarization direction. The theoretical data shows ionization yield differences for energetic electrons along the probe-laser polarization axis between C atoms with $M_L = 1$ and $M_L = 0$ at zero time delay.

ionization peaks drop off rapidly with increasing energy. For $M_L = 1$, however, after a sharp drop for the second peak, the drop-off for higher peaks is significantly slower. The origin probably lies with the dominant m_ℓ-value of the ejected electron. For $M_L = 0$, this is $m_\ell = \pm 1$, but it is $m_\ell = 0$ for $M_L = 1$. Since $m_\ell = 0$ electrons respond more strongly to the laser field than $m_\ell = \pm 1$ electrons, it is not unexpected to see additional absorption peaks in the 2p emission spectrum for $M_L = 1$.

Figure 4 shows the photoelectron spectrum associated with the residual C^+ ion left in its lowest excited state for initial C atoms in either $M_L = 0$ or $M_L = 1$. This figure demonstrates that the probability of emission of a 2s electron has increased for $M_L = 1$ compared to $M_L = 0$, even though the 2s emission is not visible for $M_L = 1$ in figure 2. The structure of the ejected-electron energy spectrum has changed, with the peaks for above-threshold ionization now less visible for $M_L = 1$ compared to $M_L = 0$. In addition, the peak at 4 eV appears to be affected by an interference effect for $M_L = 0$, whereas no such effect is seen for $M_L = 1$. The origin of this interference structure is unclear. The inclusion of higher-lying thresholds ensures that C resonances can be present at this energy, but only states of $^3S^e$ symmetry would be accessible for $M_L = 0$ and not for $M_L = 1$.

The ejected-electron momentum distributions shown in figures 1 and 2 can be used to model the influence of spin-orbit dynamics. In experiment [4, 5], an electron is detached from C^- to leave a residual C atom. This C atom is in a superposition of the different J-levels of the $2s^2 2p^2$ ground state, and this superposition will evolve in time due to the spin-orbit splitting of the different J levels. The evolution of the C atom is measured experimentally by examining the dependence of the emission of high-energy electrons along the laser polarization axis on time delay. The polarization axis of the C^- photodetachment laser is varied between perpendicular and parallel

polarization, and the dynamics is determined by examining the difference in C^+ yield along the probe laser polarization axis between the two polarizations for the pump laser.

In our theoretical model, we assume that the pump laser detaches the $m_\ell = 0$ electron from the $2p^3$ $^4S^o$ ground state of a initial C^- ion, leaving a C atom in its ground state with $M_L = 0$. For parallel polarization of the probe laser, the initial state at zero time-delay is thus an $M_L = 0$ state, whereas for perpendicular polarization, the initial state is in a superposition of $M_L = 1$ and $M_L = -1$. We can then project the $^3P^e$ initial state with quantum numbers L, M_L, S, M_S onto the J, M_J sublevels. We then propagate these J, M_J sublevels in time according to the energy splittings given in the literature [9]. After a time delay, we project back onto the L, M_L, S, M_S sublevels and use the population in the different M_L levels to predict the ejected-electron momentum distribution. The emission within a cone of $11.7°$ from the laser polarization axis, with a minimum magnitude for the momentum of 0.4 atomic units, similar to experiment [4, 5], is then taken as the high-energy ionization yield along the laser polarization direction for both the initial state in $M_L = 0$ or in the superposition for $M_L = \pm 1$. The propagation of the C ground state during the time delay can give rise to three beat periods in the picosecond range, $\tau_1 = 1235$ fs, $\tau_2 = 769$ fs, and $\tau_3 = 2034$ fs.

Figure 5 shows re-scaled normalised high-energy ionization yield differences, similar to the definition used in the experimental study [5],

$$S(\tau) = \frac{S_{\pm 1}(\tau) - S_0(\tau)}{S_{\pm 1}(\tau) + S_0(\tau)}, \tag{1}$$

where $S_{\pm 1}(\tau)$ is the high-energy ionization yield along the laser polarization axis obtained for the initial superposition of $M_L = \pm 1$ at a time delay τ, and $S_0(\tau)$ the same obtained for $M_L = 0$. The high-energy ionization yields have been rescaled to match up with the experimental results in overall variation of the normalised yields, zero yield position, and zero time delay. The first reason for this rescaling is that the experimental study was carried out at signficantly different experimental conditions: the wavelength was 1310 nm, and the peak intensity was estimated to be 4×10^{14} W/cm^2. This may lead to significant differences in the actual ionization yields. The second reason is the assumption of pure $m_\ell = 0$ emission by the pump pulse. Although the emission of $m_\ell = 0$ electrons should dominate, some $m_\ell = \pm 1$ electron will also be emitted. However, these differences will not affect the fundamental character of the dynamics induced by the spin-orbit interaction: the same dynamics should be observed in both theory and experiment.

Figure 5 indeed shows excellent agreement between the experimentally observed effect of spin-orbit dynamics on the ejected-electron momentum distributions and the theoretical model. This demonstrates that it is appropriate to separate the dynamics induced by the laser field from the dynamics induced by the spin-orbit interaction for this particular investigation. The good agreement further demonstrates that the main physical reason that the spin-orbit dynamics can be observed in this scheme, is that the emission of 2p electron with $m_\ell = 0$ is forbidden when the C atom is in a state with $M_L = 0$.

IV. CONCLUSIONS

We have developed capability within the R-matrix with time dependence approach to investigate multiphoton ionization of general atoms with non-zero initial magnetic quantum number. The size of the calculations approximately double due to the need to take both parities into account for each angular momentum. We demonstrate the capability of the approach by investigating multiphoton ionization of ground-state C atoms at a

wavelength of 390 nm. The ejected-electron momentum distributions show that both 2p and 2s electrons can be ejected during the process with the emission of 2s electrons gaining in importance for initial $M_L = 0$ compared to $M_L = 1$. For an initial state with $M_L = 0$, emission of 2p electrons can not occur along the laser polarization axis, and this provides an excellent means of demonstrating the dynamics induced by spin-orbit coupling in the C ground state. A theoretical model of this dynamics shows excellent agreement with the experimentally observed dynamics.

In the calculations, we have used significant expansion lengths in the description of C. We have used 8 target states and a maximum angular momentum $L_{\max} = 53$. The calculations demonstrate that the RMT codes are capable of handling larger basis sets and more extensive angular-momentum expansions, including outer-region expansions of well over 1000 channels. Application of the RMT codes to problems involving significant CI expansions in the inner region is therefore possible. This would be important for the detailed treatment of ultrafast processes in inner shells, where changes to the outer-electron orbitals following inner-shell emission may have to be included.

V. ACKNOWLEDGEMENTS

[1] F. Krausz and M. Ivanov, *Rev. Mod. Phys.* **81**, 163 (2009).

[2] A. Fleischer *et al*, *Phys. Rev. Lett.* **107**, 113003 (2011).

[3] E. Goulielmakis *et al*, *Nature (London)* **466**, 739 (2010).

[4] H. Hultgren, M. Eklund, D. Hanstorp, I. Yu. Kiyan, *Phys. Rev. A* **87**, 031404(R) (2013).

[5] M. Eklund, H. Hultgren, D. Hanstorp, I. Yu. Kiyan, *Phys. Rev. A* **88**, 023423(R) (2013).

[6] E. Sokell, S. Zamith, M.A. Bouchene, and B. Girard, *J. Phys. B* **33**, 2005 (2000).

[7] A. C. Brown and H.W. van der Hart, *Phys. Rev. A* **88**, 033419 (2013).

[8] O. Hassouneh, A. C. Brown, and H.W. van der Hart

Phys. Rev. A **89**, 033409 (2014).

[9] C.E. Moore, in *CRC Series in Evaluated Data in Atomic Physics*, 339pp. (Ed. J.W. Gallagher, CRC Press, Boca Raton, FL 1993)

[10] N. Rohringer and R. Santra, *Phys. Rev. A* **79**, 053402 (2009).

[11] S. Pabst, A. Sytcheva, A. Moulet, A. Wirth, E. Goulielmakis and R. Santra, *Phys. Rev. A* **86**, 063411 (2012)

[12] L.A.A. Nikolopoulos, J.S. Parker and K.T. Taylor, *Phys. Rev. A* **78**, 063420 (2008).

[13] M. A. Lysaght, H. W. van der Hart and P. G. Burke, *Phys. Rev. A* **79**, 053411 (2009).

[14] M. A. Lysaght, L. R. Moore, L. A. A. Nikolopoulos, J. S.

Parker, H. W. van der Hart, and K. T. Taylor, *Quantum Dynamic Imaging: Theoretical and Numerical Methods* Eds. A. D. Bandrauk and M. Ivanov (Springer, Berlin, 2011), pp. 107–134.

[15] L. R. Moore, M.A. Lysaght, L.A.A. Nikolopoulos, J.S. Parker, H.W. van der Hart and K.T. Taylor, *J. Mod. Opt.* **58**, 1132 (2011).

[16] S. Hutchinson, M.A. Lysaght and H.W. van der Hart, *J. Phys. B* **44**, 215602 (2011)

[17] L. R. Moore, M.A. Lysaght, J.S. Parker, H.W. van der Hart and K.T. Taylor, *Phys. Rev. A* **84**, 061404 (2011).

[18] H.W. van der Hart, *Phys. Rev. A* **89**, 053407 (2014)

[19] P. G. Burke and K. A. Berrington, *Atomic and Molecular processes: An R-matrix approach* (IOP publishing, Bristol, 1993).

[20] P. G. Burke, *R-Matrix Theory of Atomic Collisions* (Springer, Heidelberg, 2011).

[21] E.S. Smyth, J. S. Parker and K. T. Taylor, *Comp. Phys. Comm.* **114** 1 (1998).

[22] P. G. Burke and K. T. Taylor, *J. Phys. B: At. Mol. Phys.* **12**, 2971 (1979).

[23] E. Clementi and C. Roetti, *At. Data Nucl. Data Tables* **14**, 177 (1974).